Control of Andreev Bound States Using Superconducting Phase Texture

Abhishek Banerjee,[1] Max Geier,[1] M. Ahnaf Rahman,[1] Daniel S. Sanchez,[1] Candice Thomas,[2] Tian Wang,[2]
Michael J. Manfra,[2,3] Karsten Flensberg,[1] and Charles M. Marcus[1]

[1]Center for Quantum Devices, Niels Bohr Institute, University of Copenhagen, Universitetsparken 5, 2100 Copenhagen, Denmark
[2]Department of Physics and Astronomy and Birck Nanotechnology Center, Purdue University, West Lafayette, Indiana 47907, USA
[3]School of Materials Engineering and Elmore Family School of Electrical and Computer Engineering, Purdue University,
West Lafayette, Indiana 47907, USA

Andreev bound states with opposite phase-inversion asymmetries are observed in local tunneling spectra at the two ends of a superconductor-semiconductor-superconductor planar Josephson junction in the presence of a perpendicular magnetic field, while the nonlocal spectra remain phase symmetric. Spectral signatures agree with a theoretical model, yielding a physical picture in which phase textures in superconducting leads localize and control the position of Andreev bound states in the junction, demonstrating a simple means of controlling the position and size of Andreev states within a planar junction.

The manipulation of spatial properties of Andreev bound states (ABSs), both their position and spatial extent, is an important goal in contemporary superconducting physics. For instance, several physical braiding protocols that can test exotic exchange statistics, including certain constructions of a topological quantum processor, rely on spatially exchanging the positions of Majorana zero modes (MZMs) [1–4]. While measurement-based braiding protocols of MZMs have also been proposed [5–7], experimental progress in that direction is limited. The spatial extent of ABSs is also a key parameter that determines the coupling of states in Andreev molecules [8,9], Majorana chains, and quantum-dot states interacting via superconductors [10–12]. A general method for spatially manipulating ABSs, which is also fast and hysteresis-free, is highly sought after. In this direction, previous works have suggested the use of chemical potential [2] and magnetic field texture [13–15] for spatial control of ABSs. Experimentally, an array of electrostatic gates has been used for local ABS control [16,17].

Controllable superconducting phase provides an additional useful knob for ABS manipulation. In bulk superconductors, Abrikosov and Pearl vortices [18,19] represent windings of the superconducting phase that can trap ABSs, including MZMs [20,21]. Spatial manipulation of individual vortices has been demonstrated [22–27]. Similarly, Josephson vortices arising from phase windings in superconductor-normal-superconductor (SNS) junctions, are also amenable to spatial manipulation [28–32] and can host MZMs [33–35]. In planar Josephson junctions (PJJs), recent proposals have suggested that superconducting phase textures, not necessarily in a vortex configuration, can be used to spatially control MZMs and even execute

braiding operations [34–36]. Encouraging progress has been made toward realizing topological superconductivity on this platform [37–44].

In this Letter, we study PJJs consisting of SNS junctions, where N is a semiconductor with strong spin-orbit coupling. We focus on nontopological ABSs and study their response to a perpendicular magnetic field applied through the junction. A spatially varying phase texture is induced on the two superconducting leads. ABSs formed in the N region respond to this phase texture such that their localization length is controlled by the magnitude of magnetic flux penetrating the junction area and their position is controlled by a phase bias applied across the junction.

The PJJs are fabricated on InAs/Al heterostructure stacks. The N region comprises an InAs layer with Al stripped away, whereas the S regions are composed of patterned Al/InAs superconducting leads [Fig. 1(a)]. Quantum point contacts, formed by electrostatic gating, allow tunneling spectroscopy at the two ends of the junction, with the labels top or T and bot or B in Fig. 1(a) identifying the top and bottom ends, respectively. Nonlocal electrical transport between the two ends allows bulk spectroscopy [45–49]. Phase biasing of the junction is obtained by embedding in a radio-frequency superconducting quantum interference device geometry, consisting of a superconducting loop. At low perpendicular magnetic field, $|B_\perp| \sim 0.1$ mT, we observe phase-inversion-symmetric conductance spectra [Figs. 1(b)–1(e)]. As $|B_\perp|$ is increased, the local conductance spectra become phase-inversion asymmetric, with opposite phase asymmetries in the top [Figs. 1(b) and 1(c)] and bottom local conductances [Figs. 1(d) and 1(e)]. On the other hand, the nonlocal
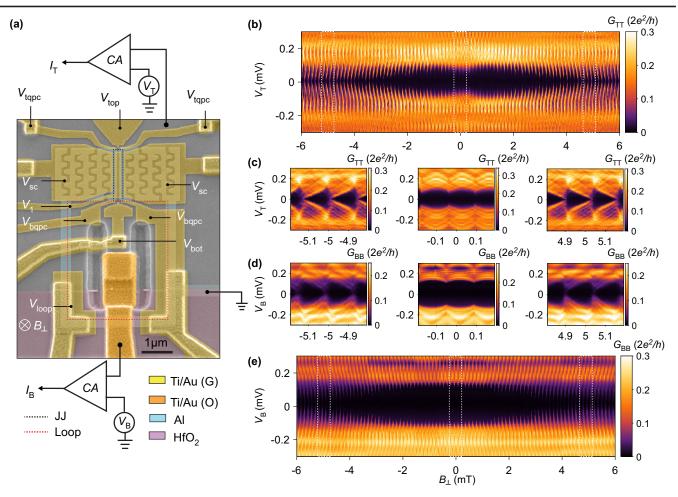
FIG. 1. Device micrograph and differential conductance as a function of perpendicular magnetic field. (a) False-color electron micrograph of a planar Josephson junction device measured in a three-terminal configuration allowing local and nonlocal tunneling spectroscopy. dc biases, V_T and V_B, are applied to top and bottom Ohmic contacts through current amplifiers (CAs) connected to the respective terminals. The superconducting loop is grounded. Gates $V_{top(bot)}$ and $V_{t(b)qpc}$ create an electrostatic constriction at the top (bottom) end for tunneling spectroscopy. V_{sc} controls density under the superconducting leads. V_1 controls density in the junction. An out-of-plane magnetic field threads magnetic flux through the device. Two distinct areas of flux penetration are identified: the Josephson junction (JJ) indicated by a black dashed rectangle and the superconducting loop indicated by the red dashed rectangle of larger size. (b), (e) Differential conductance measured at the top and bottom ends of the junction, as a function of the out-of-plane magnetic field $B_\perp$. The superconducting gap oscillates periodically, with period comparable to $\Phi_0 = h/2e$ through the superconducting loop. The magnitude of the gap at both ends is diminished as $|B_\perp|$ increases. (c) Top and (d) bottom end differential conductance spectrum showing ~ 3 flux lobes centered around (left) $B_\perp = -5$, (center) $B_\perp = 0$, and (right) $B_\perp = +5$ mT. Notice that the top and bottom conductance spectra become phase asymmetric at finite $B_\perp$, with the sense of asymmetry reversed upon changing the sign of $B_\perp$. The sense of asymmetry is opposite for the top and bottom conductance spectra.

conductance spectrum remains relatively phase symmetric within each flux lobe [Fig. 3].

This conductance fingerprint is captured by theoretical simulations. The combination of phase biasing and magnetic field penetrating the Josephson junction creates a phase texture within the two S leads, which we obtain from a Ginzburg-Landau calculation (see Supplemental Material [50]). As a result, the proximity induced gap in the N region is spatially modulated. Andreev bound states are trapped at positions along the junction where the local phase difference $\sim (2n + 1)\pi$, with n being an integer. For

every flux quantum ($\Phi_0 = h/2e$) that enters (exits) the superconducting loop, localized Andreev bound states are pumped from the outer (inner) to the inner (outer) junction end, creating phase-inversion-asymmetric conductance patterns at the two ends. Since these modes are spatially localized, they do not appear in the nonlocal conductance spectra. When the magnetic field through the junction center (defined later) exceeds Φ_0, well-localized Josephson vortices are formed.

Figure 1(a) shows an electron micrograph of one of the devices, along with a schematic electrical circuit.

The device is fabricated on a molecular-beam-epitaxy grown heterostructure with an InAs quantum well separated from a top Al layer by an $In_{0.75}Ga_{0.25}As$ barrier. A combination of wet etching of the Al layer and deep wet etching of the semiconductor stack is used to define the superconducting loop, the Josephson junction, and the mesa with a U-shaped trench. A patch of the mesa (with Al removed) within the loop is contacted by a layer of Ti/Au to form an internal submicron Ohmic contact to enable bottom-end tunneling spectroscopy. A layer of HfO_2, grown by atomic layer deposition and patterned in a rectangular shape, is used to isolate the Ti/Au layer from the superconducting loop and the conducting mesa. A second layer of HfO_2 is deposited globally followed by the deposition of Ti/Au gates for electrostatic control of the junction and the quantum point contacts (QPCs). The carrier density in the normal barrier of the JJ (width $w_n = 100$ nm, length $l = 1.6$ μm) is controlled by energizing gate voltage V_1. Gate voltage V_{sc} controls the carrier density in the semiconductor underneath the superconducting leads. Split gates controlled by voltages V_{TQPC} and V_{BQPC} electrostatically define constrictions at the top and bottom of the junction to serve as QPC tunnel barriers. Additional gates controlled by V_{top} and V_{bot} control densities in the normal regions outside the QPCs and are typically fixed at ∼100 mV. Here we focus on results from device 1; qualitatively similar results are obtained in device 2 (see Supplemental Material, Figs. S8–S10 [50]).

We first investigate local tunneling spectra at the two ends as a function of perpendicular magnetic field as shown in Fig. 1(b) (top end) and 1(e) (bottom end). We observe a superconducting gap at both ends that is periodically modulated with a periodicity of $B_\perp \simeq 0.14$ mT, corresponding to Φ_0 through the superconducting loop. The spectra also show a large scale structure with respect to $B_\perp$, where the amplitude of gap modulation is suppressed with $|B_\perp|$ (see also Figs. S6 and S7 [50]).

Focusing on the large scale gap structure, we observed that individual flux lobes acquire significant phase asymmetry as $|B_\perp|$ was increased. This is represented in Figs. 1(c) and 1(d). For flux lobes centered around $B_\perp = -5$ mT, the top-end local differential conductance G_{TT} shows a set of arrowhead-shaped features that approach zero bias at the left (more negative field) end of the lobe and become maximally gapped at the right (less negative field) end. This pattern is reversed for the bottom-end conductance spectra G_{BB}. Investigating the structure of the flux lobes at $B_\perp = +5$ mT shows that the sense of this asymmetry in flux is reversed at both ends. Flux lobes centered around $B_\perp = 0$ are left-right symmetric; that is, the gap is modulated symmetrically within each flux lobe at both ends.

To help understand this behavior, we perform theoretical simulations of the device. When subjected to a perpendicular magnetic field, identical Meissner supercurrents are set up in

the superconducting leads, leading to a spatially varying phase profile (see Supplemental Material for details [50]). We use Ginzburg-Landau equations to calculate the phase profile within the gauge $\vec{A} = -yB_\perp \hat{x}$. The phase configurations in the left (ϕ_L) and right leads (ϕ_R) obtain a $B_\perp$-dependent gradient given by $d\phi_{L/R}(x)/dx = \pm\pi d_S B_\perp/\Phi_0$, where $d_S = (w_n + w_s) = 300$ nm is the center-to-center distance between the two superconducting leads. The effect of the magnetic field through the superconducting loop is modeled as a global phase difference, $\phi_0 = 2\pi A_L B_\perp/\Phi_0$ between the two leads, where $A_L \simeq 15$ μm^2 is the effective loop area. As a result, the gauge-invariant phase difference across the junction is given as $\Delta\phi(x) = \phi_0 + (2\pi d_S B_\perp/\Phi_0)x$. The central area of the junction $A_c = d_S l$ determines the total phase winding along the junction $\Delta\phi(l) - \Delta\phi(0) = (2\pi B_\perp A_c/\Phi_0)$. Each 2π winding of the local phase difference corresponds to a Josephson vortex in the junction [30,57].

In the model, ABSs are trapped in nodes of the local phase difference, when $\Delta\phi(x_0) = \pi$ at a position x_0 along the junction. The node position x_0 can be controlled by the global phase bias ϕ_0. The localization length of the ABS along the junction, $\xi_B = \sqrt{\Phi_0/B_\perp}\sqrt{\xi_P/d_S}$, is controlled by the perpendicular magnetic field threading the junction, where ξ_P is the proximity induced coherence length (see Supplemental Material [50]). At large $B_\perp$, $\xi_B \leq l$, and well-developed Josephson vortices are formed at the nodes. The number of vortices is given by $\simeq \Phi_0/(d_S L B_\perp)$.

Using exact diagonalization of a minimal tight-binding model of the Josephson junction, we find that the nodes bind low-energy Andreev bound states. In Figs. 2(a) and 2(b), we show the local-density-of-states (LDOS) map of the lowest-energy ABS trapped within the junction, formed at $B_\perp = -5.02$ mT. Higher-energy ABSs, roughly $\simeq 2\Phi_0/(d_S B_\perp \lambda_F)$ in number, where λ_F is the Fermi wavelength, are also formed within the vortex core (see Fig. S2 [50]). Variation of the loop flux by $B_\perp$ changes the position of the node, as represented by the LDOS maps in Fig. 2(b) at different values of magnetic field centered around $B_\perp = -5$ mT. At $|B_\perp| \simeq 0$, ABSs are delocalized over the entire length of the junction [Fig. 2(c)] and exhibit spatial modulations due to the standing wave condition in the junction. The periodicity of these oscillations is roughly half the Fermi wavelength. Unlike Fraunhofer oscillations, where the critical Josephson current is minimal when the junction traps a flux quantum, we do not observe distinctive spectral signatures associated with this effect (see Figs. S2, S4, S6, and S8 in the Supplemental Material [50]).

These ABSs produce distinctive conductance signatures. We attach normal leads to the two ends of the junction and evaluate the 2×2 conductance matrix as a function of $B_\perp$ [Figs. 2(e)–2(g)]. Around $B_\perp = -5$ mT, Fig. 2(e), local conductances, G_{TT} and G_{BB}, display phase-inversion-asymmetric lobes with opposite asymmetries at the two ends. A gap minimum in G_{TT} and G_{BB} is observed when
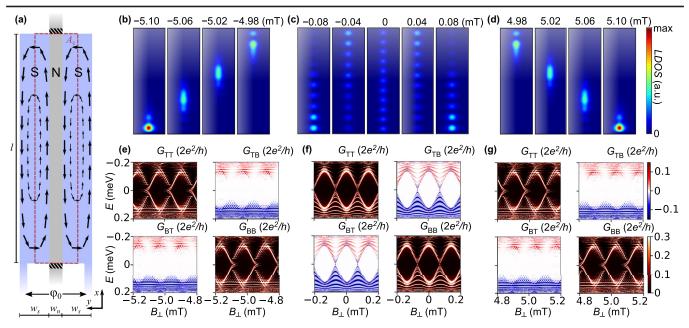
FIG. 2. Theory. (a) Schematic of the device showing supercurrent profile in the superconducting leads, of width w_s and length l, at finite $B_\perp$. Arrows correspond to the gauge-invariant local supercurrent density $\vec{j}$. A global phase difference ϕ_0 is imposed between the S leads by a superconducting loop (not shown). The normal barrier N, of width w_n, is connected by tunnel barriers to normal leads at the two ends for conductance calculations. The red dashed lines indicate the central area of the junction that determines the relative local phase difference between the top and bottom ends. (b)–(d) LDOS of the lowest-energy Andreev bound state around (b) $B_\perp = -5$, (c) $B_\perp = 0$, and (d) $B_\perp = +5$ mT, in steps of $\Delta B_\perp = 0.04$ mT. (e)–(g) Calculated conductance matrix at finite out-of-plane magnetic field around (e) $B_\perp = -5$, (f) $B_\perp = 0$, and (g) $B_\perp = 5$ mT, respectively.

the local phase difference $\Delta\phi(x) \sim \pi$ at the top ($x = l$) and bottom ($x = 0$) ends, respectively. This happens at different magnetic field values, with $\Delta B_\perp = A_c B_\perp / A_L$.

Around each gap minimum, the lowest-energy states fade at the top and reappear at the bottom as the magnitude of the magnetic field is increased. These are the strongly localized, lowest-energy modes trapped in the phase node. In contrast, nonlocal conductances, G_{TB} and G_{BT}, remain comparatively phase-inversion symmetric and do not have pronounced gap minima. The main contribution to nonlocal conductance comes from states that are extended throughout the junction [46,47] and are therefore largely unaffected by local phase differences. At $B_\perp = 0$ [Fig. 2(f)], all the junction modes are extended and the flux lobes are symmetric in both local and nonlocal conductances.

Even though our conductance calculations are performed in the clean limit, in the diffusive limit we expect similar results with a renormalized superconducting coherence length in the Al/InAs heterostructure [30]. Furthermore, we expect that spin-orbit coupling is not relevant for the central features of our data (see Supplemental Material for exact diagonalization of the vortex ABS, which are almost spin degenerate [50]). Finally, we notice that the observed phase asymmetry is stronger in the experiment compared to theory. This may be attributed to the finite inductance of the superconducting loop used for phase biasing. The phase dropped across this inductance causes a nonlinear

relationship between $B_\perp$ and the phase bias, contracting phase spectra near $\phi = \pi$ and expanding them near $\phi = 0$ (see [44]). This effect is not included in our model and may explain the larger asymmetry in experiment compared to theory.

We next consider experimental measurement of nonlocal differential conductance (see Supplemental Material [50] and Ref. [49] for details). As seen in Fig. 3, the phase-inversion asymmetry that was present in local conductances is strongly suppressed in the nonlocal spectra. For example, flux lobes centered around $B_\perp = \pm 5$ mT, shown in Figs. 3(b) and 3(c), display weak asymmetry within each flux lobe. Furthermore, states that close the spectral gap in the local spectra [Figs. 1(c) and 1(d)] are absent in nonlocal spectra.

Reasonable agreement between theoretical and experimental conductance matrix signatures supports our interpretation of spatial manipulation of ABSs with superconducting phase texture. In the presence of a finite in-plane magnetic field, Josephson junctions with strong spin-orbit coupling, such as ours, may host spin-split Andreev bound states and topologically protected Majorana zero modes [37,39]. We expect our ABS manipulation scheme to work also at finite in-plane magnetic fields, where apart from a reduction of the induced gap size, the phase response of nontopological ABSs remains qualitatively similar. However, the case of Majorana bound states
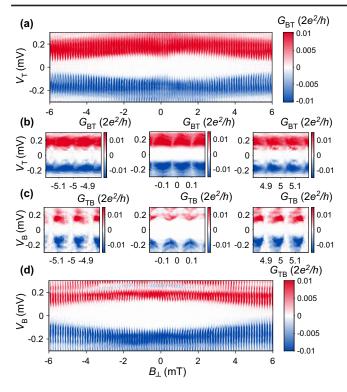
FIG. 3. Nonlocal differential conductance as a function of perpendicular magnetic field. Nonlocal differential conductances (a) G_{BT} and (d) G_{TB}, as a function of the out-of-plane magnetic field $B_\perp$. The nonlocal gap is periodically modulated with the loop flux. The magnitude of the nonlocal gap at both ends is diminished as $|B_\perp|$ increases. (b) G_{BT} and (c) G_{TB} measured for ~ 3 flux lobes centered around (left) $B_\perp = -5$, (center) $B_\perp = 0$, and (right) $B_\perp = +5$ mT. Compared to the local conductances, the nonlocal conductances are relatively phase symmetric at all values of $B_\perp$. Also, subgap states that approach zero energy in local conductances (Fig. 1) are absent in the nonlocal spectrum.

may be more complicated since the topological phase boundary is also determined by the phase profile along the junction [34,36]. Detailed experiments in the high field regime are required to go further in the direction of non-Abelian braiding and fusion-rule experiments using this scheme [34,36,58]. Future work may focus on this.

[1] C. Nayak, S. H. Simon, A. Stern, M. Freedman, and S. Das Sarma, Rev. Mod. Phys. **80**, 1083 (2008).

[2] J. Alicea, Y. Oreg, G. Refael, F. Von Oppen, and M. Fisher, Nat. Phys. **7**, 412 (2011).

[3] A. Stern and N. H. Lindner, Science **339**, 1179 (2013).

[4] A. Y. Kitaev, Ann. Phys. (Amsterdam) **303**, 2 (2003).

[5] P. Bonderson, M. Freedman, and C. Nayak, Phys. Rev. Lett. **101**, 010501 (2008).

[6] P. Bonderson, M. Freedman, and C. Nayak, Ann. Phys. (Amsterdam) **324**, 787 (2009).

[7] T. Karzig, C. Knapp, R. M. Lutchyn, P. Bonderson, M. B. Hastings, C. Nayak, J. Alicea, K. Flensberg, S. Plugge, Y. Oreg, C. M. Marcus, and M. H. Freedman, Phys. Rev. B **95**, 235305 (2017).

[8] J.-D. Pillet, V. Benzoni, J. Griesmar, J.-L. Smirr, and C. O. Girit, Nano Lett. **19**, 7138 (2019).

[9] V. Kornich, H. S. Barakov, and Y. V. Nazarov, Phys. Rev. Res. **1**, 033004 (2019).

[10] T.-P. Choy, J. M. Edge, A. R. Akhmerov, and C. W. J. Beenakker, Phys. Rev. B **84**, 195442 (2011).

[11] J. D. Sau and S. D. Sarma, Nat. Commun. **3**, 964 (2012).

[12] F. Pientka, L. I. Glazman, and F. von Oppen, Phys. Rev. B **88**, 155420 (2013).

[13] M. Kjaergaard, K. Wölms, and K. Flensberg, Phys. Rev. B **85**, 020503(R) (2012).

[14] J. Klinovaja and D. Loss, Phys. Rev. X **3**, 011008 (2013).

[15] G. L. Fatin, A. Matos-Abiague, B. Scharf, and I. Žutić, Phys. Rev. Lett. **117**, 077002 (2016).

[16] B. H. Elfeky, N. Lotfizadeh, W. F. Schiela, W. M. Strickland, M. Dartiailh, K. Sardashti, M. Hatefipour, P. Yu, N. Pankratova, H. Lee, V. E. Manucharyan, and J. Shabani, Nano Lett. **21**, 8274 (2021).

[17] A. Pöschl, A. Danilenko, D. Sabonis, K. Kristjuhan, T. Lindemann, C. Thomas, M. J. Manfra, and C. M. Marcus, Phys. Rev. B **106**, L161301 (2022).

[18] A. A. Abrikosov, Sov. Phys. JETP **5**, 1174 (1957).

[19] J. Pearl, Appl. Phys. Lett. **5**, 65 (1964).

[20] D. A. Ivanov, Phys. Rev. Lett. **86**, 268 (2001).

[21] L. Fu and C. L. Kane, Phys. Rev. Lett. **100**, 096407 (2008).

[22] B. W. Gardner, J. C. Wynn, D. Bonn, R. Liang, W. Hardy, J. R. Kirtley, V. G. Kogan, and K. A. Moler, Appl. Phys. Lett. **80**, 1010 (2002).

[23] E. W. Straver, J. E. Hoffman, O. M. Auslaender, D. Rugar, and K. A. Moler, Appl. Phys. Lett. **93**, 172514 (2008).

[24] O. M. Auslaender, L. Luan, E. W. Straver, J. E. Hoffman, N. C. Koshnick, E. Zeldov, D. A. Bonn, R. Liang, W. N. Hardy, and K. A. Moler, Nat. Phys. **5**, 35 (2009).

[25] N. Shapira, Y. Lamhot, O. Shpielberg, Y. Kafri, B. J. Ramshaw, D. A. Bonn, R. Liang, W. N. Hardy, and O. M. Auslaender, Phys. Rev. B **92**, 100501(R) (2015).

[26] A. Kremen, S. Wissberg, N. Haham, E. Persky, Y. Frenkel, and B. Kalisky, Nano Lett. **16**, 1626 (2016).

[27] J.-Y. Ge, V. N. Gladilin, J. Tempere, C. Xue, J. T. Devreese, J. Van de Vondel, Y. Zhou, and V. V. Moshchalkov, Nat. Commun. **7**, 13880 (2016).

[28] M. Tinkham, *Introduction to Superconductivity*, 2nd ed., International Series in Pure and Applied Physics (McGraw-Hill, New York, 1996).

[29] K. K. Likharev, Rev. Mod. Phys. **51**, 101 (1979).

[30] D. Roditchev, C. Brun, L. Serrier-Garcia, J. C. Cuevas, V. H. L. Bessa, M. V. Milošević, F. Debontridder, V. Stolyarov, and T. Cren, Nat. Phys. **11**, 332 (2015).

[31] G. Carapella, P. Sabatino, C. Barone, S. Pagano, and M. Gombos, Sci. Rep. **6**, 1 (2016).

[32] V. V. Dremov, S. Y. Grebenchuk, A. G. Shishkin, D. S. Baranov, R. A. Hovhannisyan, O. V. Skryabina, N. Lebedev, I. A. Golovchanskiy, V. I. Chichkov, C. Brun *et al.*, Nat. Commun. **10**, 1 (2019).

[33] E. Grosfeld and A. Stern, Proc. Natl. Acad. Sci. U.S.A. **108**, 11810 (2011).

[34] A. Stern and E. Berg, Phys. Rev. Lett. **122**, 107701 (2019).

[35] X. Ma, C. J. O. Reichhardt, and C. Reichhardt, Phys. Rev. B **101**, 024514 (2020).

[36] T. Zhou, M. C. Dartiailh, W. Mayer, J. E. Han, A. Matos-Abiague, J. Shabani, and I. Žutić, Phys. Rev. Lett. **124**, 137001 (2020).

[37] M. Hell, M. Leijnse, and K. Flensberg, Phys. Rev. Lett. **118**, 107701 (2017).

[38] M. Hell, K. Flensberg, and M. Leijnse, Phys. Rev. B **96**, 035444 (2017).

[39] F. Pientka, A. Keselman, E. Berg, A. Yacoby, A. Stern, and B. I. Halperin, Phys. Rev. X **7**, 021032 (2017).

[40] A. Fornieri, A. M. Whiticar, F. Setiawan, E. Portolés, A. C. Drachmann, A. Keselman, S. Gronin, C. Thomas, T. Wang, R. Kallaher *et al.*, Nature (London) **569**, 89 (2019).

[41] H. Ren, F. Pientka, S. Hart, A. T. Pierce, M. Kosowsky, L. Lunczer, R. Schlereth, B. Scharf, E. M. Hankiewicz, L. W. Molenkamp *et al.*, Nature (London) **569**, 93 (2019).

[42] M. C. Dartiailh, W. Mayer, J. Yuan, K. S. Wickramasinghe, A. Matos-Abiague, I. Žutić, and J. Shabani, Phys. Rev. Lett. **126**, 036802 (2021).

[43] C. T. Ke, C. M. Moehle, F. K. de Vries, C. Thomas, S. Metti, C. R. Guinn, R. Kallaher, M. Lodari, G. Scappucci, T. Wang *et al.*, Nat. Commun. **10**, 3764 (2019).

[44] A. Banerjee, O. Lesser, M. A. Rahman, H.-R. Wang, M.-R. Lee, A. Kringhøj, A. M. Whiticar, A. C. C. Drachmann, C. Thomas, T. Wang, M. J. Manfra, E. Berg, Y. Oreg, A. Stern, and C. M. Marcus, arXiv:2201.03453.

[45] T. O. Rosdahl, A. Vuik, M. Kjaergaard, and A. R. Akhmerov, Phys. Rev. B **97**, 045421 (2018).

[46] J. Danon, A. B. Hellenes, E. B. Hansen, L. Casparis, A. P. Higginbotham, and K. Flensberg, Phys. Rev. Lett. **124**, 036801 (2020).

[47] G. C. Ménard, G. L. R. Anselmetti, E. A. Martinez, D. Puglia, F. K. Malinowski, J. S. Lee, S. Choi, M. Pendharkar, C. J. Palmstrøm, K. Flensberg, C. M. Marcus, L. Casparis, and A. P. Higginbotham, Phys. Rev. Lett. **124**, 036802 (2020).

[48] G. L. R. Anselmetti, E. A. Martinez, G. C. Ménard, D. Puglia, F. K. Malinowski, J. S. Lee, S. Choi, M. Pendharkar, C. J. Palmstrøm, C. M. Marcus, L. Casparis, and A. P. Higginbotham, Phys. Rev. B **100**, 205412 (2019).

[49] A. Banerjee, O. Lesser, M. A. Rahman, C. Thomas, T. Wang, M. J. Manfra, E. Berg, Y. Oreg, A. Stern, and C. M. Marcus, Phys. Rev. Lett. **130**, 096202 (2023).

[50] See Supplemental Material at http://link.aps.org/supplemental/10.1103/PhysRevLett.130.116203 for details of device fabrication, measurement, additional experimental data and theoretical modelling, which includes Refs. [51–56].

[51] J. R. Clem, Phys. Rev. B **81**, 144515 (2010).

[52] C. Kittel, *Introduction to Solid State Physics*, 8th ed. (Wiley, New York, 2004).

[53] J. Romijn, T. M. Klapwijk, M. J. Renne, and J. E. Mooij, Phys. Rev. B **26**, 3648 (1982).

[54] C. W. Groth, M. Wimmer, A. R. Akhmerov, and X. Waintal, New J. Phys. **16**, 063065 (2014).

[55] W. L. McMillan, Phys. Rev. **175**, 537 (1968).

[56] M. Istas, C. Groth, A. R. Akhmerov, M. Wimmer, and X. Waintal, SciPost Phys. **4**, 26 (2018).

[57] J. C. Cuevas and F. S. Bergeret, Phys. Rev. Lett. **99**, 217002 (2007).

[58] S. S. Hegde, G. Yue, Y. Wang, E. Huemiller, D. Van Harlingen, and S. Vishveshwara, Ann. Phys. (Amsterdam) **423**, 168326 (2020).